ROYAL SOCIETY
OF CHEMISTRY

PAPER

Check for updates

A solution to break the salt barrier for high-rate sustainable solar desalination†

Lin Zhu, [ID][a] Lei Sun,[a] Hong Zhang,[b] Hüsnü Aslan,[c] Ye Sun, [ID][b] Yudong Huang,[a] Federico Rosei [ID][d] and Miao Yu [ID]*[a]

Solar steam generation (SSG) is a promising approach to address the global shortage of freshwater by seawater treatment, but commonly suffers from salt-accumulation related issues, drastically reducing the operational efficiency and lifetime of SSG systems. Herein, we propose a strategy for sustainable SSG from seawater, enabling powerful self-salt-discharge and self-water-pumping by constructing a closed loop between water and salt. As a result, besides an evaporation rate as high as 2.8 kg m^{-2} h^{-1} (under one sun), neither salt accumulation nor evaporation rate decline is observed upon long-term cycling of over one month or constant floating on seawater over eight months. Even upon continuous desalination in a highly concentrated solution (20 wt% NaCl) for over 400 h or under high-intensity irradiation for over 12 h, the high evaporation rate is successfully maintained. This work thus provides an effective solution for salt accumulation, addressing the top challenge for long-term sustainable desalination.

Broader context

The grave shortage of freshwater has been an unavoidable difficulty in the development of the society and economy. Addressing this challenge based on sustainable energy is desirable. In this regard, solar steam generation (SSG) from seawater has demonstrated particularly amazing promise. However, the real-life application prospect of solar desalination has been largely compromised by salt accumulation. While performance is good in deionized water, significant salt precipitation and hence a drop in SSG efficiency typically cripples operation within just a few hours upon desalination, especially for systems with relatively high evaporation rate. Therefore, aside from chasing a higher evaporation rate in clean water, achieving effective solution to salt accumulation is of paramount importance. Herein, we present a strategy to break the salt barrier for sustainable solar desalination, by constructing an efficient water–salt loop and employing a highly porous, super-hydrophobic material with competent light-harvesting and photothermal conversion capability. This work may inspire the development of a variety of advanced SSG systems with both high evaporation rate and long-term operation life.

Introduction

Among the 17 Sustainable Development Goals (SDGs), SDG n.6 (Clean Water and Sanitation) is quite prominent since water is at the basis of life on earth and is in fact crucial for other SDGs including no hunger (SDG2) and health (SDG3). In this context, energy-efficient technologies have been shown to be promising

to address the global freshwater shortage by removing salt from the seawater.[1–5] Among many desalination methods (*e.g.* reverse osmosis, capacitive deionization, membrane distillation), solar steam generation (SSG), which employs photothermal conversion materials (PCMs) to transform solar energy into heat for water steaming, has been acknowledged to be particularly practical and sustainable.[6–9]

To improve SSG systems, great efforts have been focused on developing high performance PCMs, such as metallic nanoparticles,[10,11] inorganic semiconductors,[12–14] organic polymers and carbon materials.[15–19] However, salt accumulation remains the bottleneck in SSG development. Upon desalination of seawater, salt builds up within SSG systems, blocking sunlight, reducing photothermal conversion efficiency and eventually rendering the whole system useless by clogging channels for water supply and vapour release.[20–22] While performance is good in deionized water, significant salt precipitation and

[a] *State Key Laboratory of Urban Water Resource and Environment, School of Chemistry and Chemical Engineering, Harbin Institute of Technology, Harbin 150001, China. E-mail: miaoyu_che@hit.edu.cn*

[b] *Institute of Condensed Matter Physics, School of Instrumentation Science and Engineering, Harbin Institute of Technology, Harbin 150001, China*

[c] *iNANO Centre, Aarhus University, Aarhus 8000, Denmark*

[d] *INRS Centre for Energy, Materials and Telecommunications, 1650 Boul. Lionel Boulet, Varennes J3X 1S2, Canada*

† Electronic supplementary information (ESI) available. See DOI: 10.1039/d1ee00113b

hence a drop in SSG efficiency typically cripples operation within just a few hours upon desalination,[20,23,24] especially for systems with relatively high evaporation rate.[25] Addressing salt accumulation is, therefore, of great importance to improve the performance of SSG from seawater.

Three main strategies have been used to resolve this issue. The first is periodical cleaning to physically remove the precipitated salt on PCMs.[21,26] This method requires labour, costs associated with systems' maintenance, disruption in SSG operation and can cause structural damage as well as subsequent PCMs mass loss upon cleaning. The second is to employ a designed evaporation system with aligned milli/micro-scale channel-like structures; this method can avoid the disadvantages mentioned above, and improve SSG performance by enhancing water supply and transporting salt from the absorber surface to the bulk seawater.[27-29] The third is based on the use of hydrophobic PCMs to prevent brine from reaching the evaporator surface[30,31] or using contactless solar steam generation setup.[9] Despite the major success, the evaporation rate of the SSG systems for sustainable desalination reported so far is relatively low and the operation stability is limited. Under one sun (0.1 W cm^{-2}), the best long-term stable cycling performance ever reported is 100 h desalination at a rate of 1.04 kg m^{-2} h^{-1} in highly concentrated seawater (20 wt%),[32] and 600 h desalination at an evaporation rate of $\sim$1.42 kg m^{-2} h^{-1} in seawater with normal salinity (3.5 wt%).[33] Simultaneously achieving long-term sustainability and high evaporation rate, especially in high salinity solution, remains the top challenge of solar desalination.

Herein we introduce a high-rate, sustainable SSG system with self-salt-discharge and water-pumping functions, to address the salt accumulation challenge. We use α-phase molybdenum carbide nanocrystals embedded carbon bouquets (α-MoC$_{1-x}$@CB, Fig. 1) as PCM. Our strategy consists in applying a hydrophilic cotton-mesh cylinder with one end attached to the upper edge of the cone and the other end dipped in the seawater (Fig. 1). As salt has a tendency to accumulate on the upper edge of the cone, the cylinder constructs transport bridges between the high-salinity area of the evaporator and the low-salinity area (bulk seawater). Driven by the salinity difference, efficient self-salt discharge from the evaporator to the bulk seawater and enhanced self-water pumping from seawater to the evaporator surface are enabled, forming a salt–water loop. Meanwhile, the super-hydrophobicity of α-MoC$_{1-x}$@CB prevents salt deposition in the PCM layer and further benefits salt discharge. Thanks to the competent light-harvesting and photothermal conversion capability, ultrathin α-MoC$_{1-x}$@CB film with an ultralow PCM load can already induce rapid, significant temperature rise. Both the highly porous morphology and the ultra-thin thickness of the α-MoC$_{1-x}$@CB film provide convenient path for steam evaporation. As a result, upon over one month cycling at an evaporation rate as high as 2.8 kg m^{-2} h^{-1} (under one sun illumination), we did not observe salt accumulation nor a decline in the evaporation rate. Remarkably, even after over 400 h continuous desalination in a highly concentrated salt solution (20 wt% NaCl) or after over eight months floating in a seawater container, this high evaporation rate was retained, without salt blockage. Moreover, at a much higher evaporation rate of 6.0 kg m^{-2} h^{-1} (three sun irradiation), the evaporation system showed no degradation upon 12 h continuous desalination. These long-term sustainability desalination results represent the best SSG performance ever reported from seawater (see Table S1, ESI†). Moreover, the high performance was
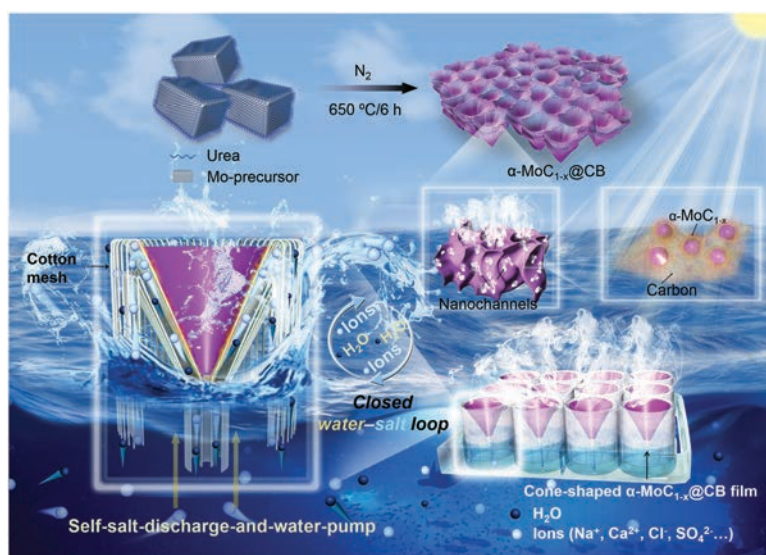

Fig. 1 Illustration of α-MoC$_{1-x}$@CB-based evaporator with the water–salt loop for solar desalination. α-MoC$_{1-x}$@CB is synthesized by producing the Mo-precursor at room temperature then carbonizing the precursor in N$_2$, resulting in a distinct bouquet morphology. Each flower-like motif is highly porous and composed of α-MoC$_{1-x}$ nanocrystals embedded carbonaceous petals, possessing efficient photothermal conversion capability and rapid path for vapour. By applying a hydrophilic cotton-mesh cylinder with one end attached to the upper edge of the cone-shaped evaporator and the other end dipped in the seawater, a bridge is constructed between the high and low salinity areas. Driven by the salinity difference, the setup enables efficient self-salt discharge and self-water pumping, forming a salt–water loop for sustainable solar desalination.

2452 | *Energy Environ. Sci.*, 2021, **14**, 2451–2459

This journal is © The Royal Society of Chemistry 2021

achieved with an ultralow PCM load (0.066 mg cm^{-2}) which is over one order of magnitude lower than the commonly used load.[20]

Results

The fabrication of α-MoC$_{1-x}$@CB involves two simple steps, *i.e.* synthesizing the Mo-precursor at room temperature and carbonizing the obtained precursor in N$_2$ (details in Methods, ESI†). Scanning Electron Microscopy (SEM) imaging (Fig. 2a and Fig. S1, ESI†) showed that the product had a unique bouquet morphology, composed of delicate flowers with porous, curved petals. Atomic Force Microscopy (AFM, Fig. 2b), Transmission Electron Microscopy (TEM, Fig. 2c and ESI†) and high-resolution TEM (HRTEM) images (Fig. 2d and e) revealed that the petals were rather thin ($\sim$3 nm in thickness), containing abundant pores, with uniformly embedded well-crystallized nanoparticles ($\sim$3 nm). Nitrogen adsorption–desorption isotherm (Fig. 2f) and pore size distribution curve (inset of Fig. 2f) indicated a high density of meso/macropores ($\sim$3 nm and 50 nm) in the sample, deducing a high specific surface area of 327.3 m^2 g^{-1} and a big pore volume of 3.2 cm^3 g^{-1}.

The thin petals and the nanocrystals were revealed to be nitrogen-doped amorphous carbon and α-MoC$_{1-x}$, respectively, based on the composition analysis using X-ray Diffraction (XRD),

Thermogravimetry (TG), Raman Spectroscopy, X-ray Photoelectron Spectroscopy (XPS), and elemental mapping results described hereafter. The broad diffraction peaks in the XRD pattern (Fig. 3a) were well indexed to α-MoC$_{1-x}$ (JCPDS No. 89-2868). Consistently, the lattice spacings of the nanocrystals in the HRTEM image (Fig. 2e) were estimated to be 0.24 and 0.21 nm, matching that of the (111) and (200) facets of α-MoC$_{1-x}$, respectively. According to TG analysis (Fig. 3b), the remaining weight of MoO$_3$ after heating to 750 K in air-flow was 82%, deducing the Mo content of 55 wt%. In the Raman spectrum (Fig. 3c), the signal around 665 cm^{-1} and those below 300 cm^{-1} originate from the vibrations of C and Mo,[34] respectively; the two pronounced vibration peaks around 1350 and 1600 cm^{-1} are assigned to the characteristic bands of carbonaceous materials, and their relative intensity suggests that the carbon species are amorphous.

XPS then unravelled more details of the chemical structure. The C 1s peak (Fig. 3d) can be deconvoluted into three sub-peaks located at 284.3, 284.7 and 285.2 eV corresponding to Mo–C, C–C and C–N bonding, respectively, suggesting the existence of MoC$_{1-x}$ and N-doped carbon in the sample. Moreover, the Mo 3d XP spectrum (Fig. 3e) exhibited three peaks, containing four distinct components corresponding to Mo^{2+} in Mo–C (indigo curve), Mo^{3+} in Mo–N (army-green curve),[35] and oxidation states of Mo^{4+} (orange curve) and
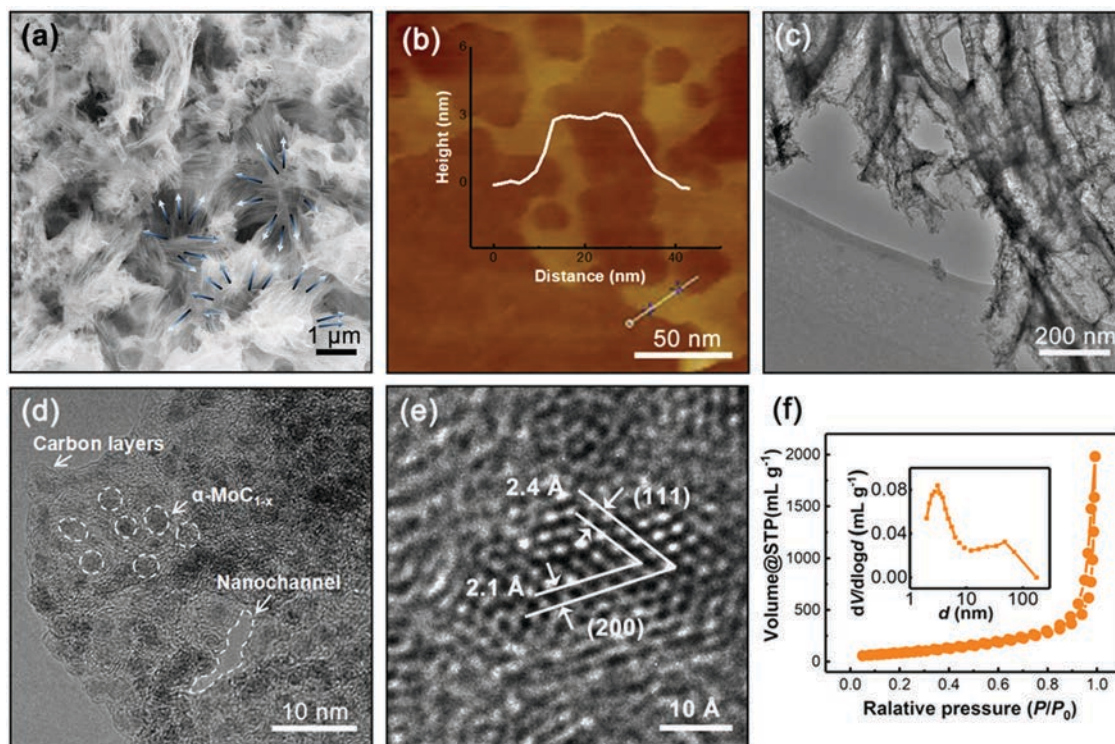

Fig. 2 Morphology and structure of α-MoC$_{1-x}$@CB. (a) SEM image of α-MoC$_{1-x}$@CB showing a distinct bouquet morphology, where the 3D flowers-like architectures possess delicate, thin petals (the arrows are superimposed to indicate the petals). (b) Height image of the petals recorded using AFM, where the superimposed curve corresponding to the linescan marked on the lower right indicates a petal thickness of $\sim$3 nm. (c) TEM, (d) and (e) HRTEM images of the α-MoC$_{1-x}$@CB petals, revealing that the half-transparent petals are porous with embedded nanocrystals in a size of $\sim$3 nm, and the interlayer spacing of 0.24 and 0.21 nm matches that of the (111) and (200) α-MoC$_{1-x}$ facets. (f) Nitrogen adsorption–desorption isotherm and pore-size distribution (inset) of α-MoC$_{1-x}$@CB, indicating that the sample is rich in mesopores ($\sim$3 nm) and macropores ($\sim$50 nm).
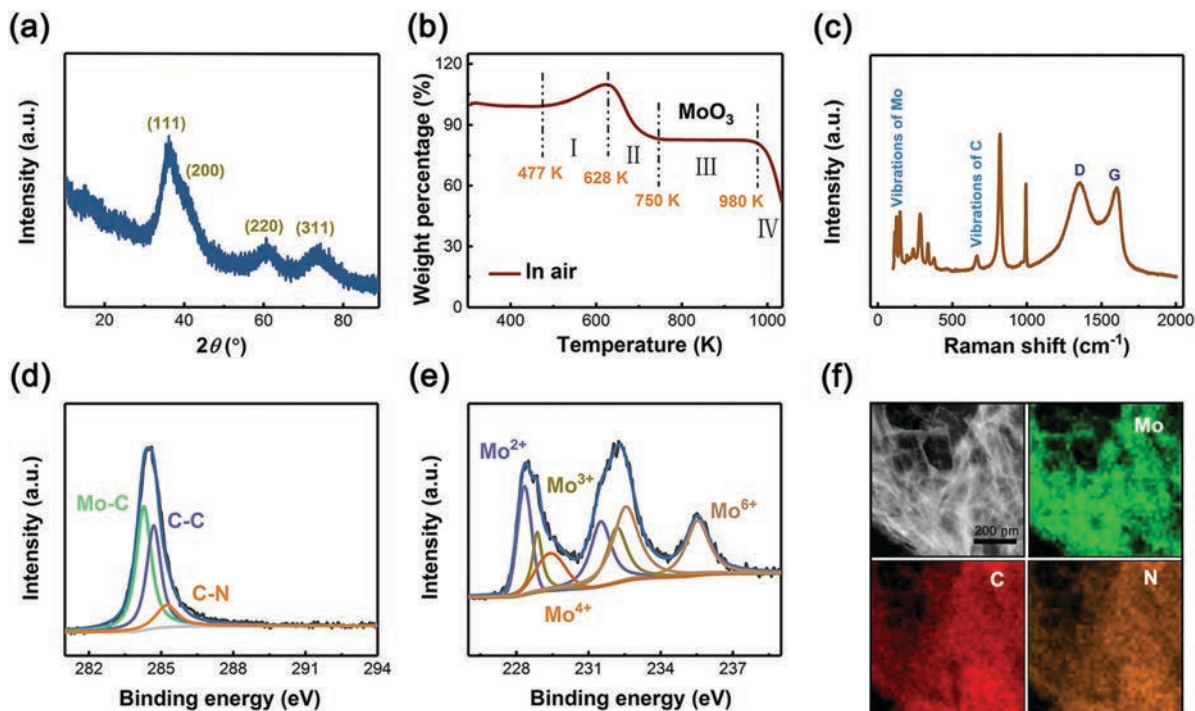
Fig. 3 Composition analysis of the α-MoC$_{1-x}$@CB. (a) XRD pattern showing broad diffraction peaks well indexed to α-MoC$_{1-x}$. (b) TG curve of α-MoC$_{1-x}$@CB, where the remaining weight of MoO$_3$ after heating to 750 K is 82%, suggesting the Mo content of 55 wt%. (c) Raman spectrum of α-MoC$_{1-x}$@CB, where the vibrations around 665 cm^{-1} and those below 300 cm^{-1} are primarily attributed to C and Mo, respectively; the pronounced peaks at 1350 and 1600 cm^{-1} are attributed to carbonaceous composition. (d) C 1s and (e) Mo 3d XP spectra of α-MoC$_{1-x}$@CB, showing the Mo–C, C–C, C–N and Mo–N bonding. (f) Elemental mapping of α-MoC$_{1-x}$@CB, where the distribution of Mo, C, and N elements suggests the uniform distribution and high density of α-MoC$_{1-x}$ nanocrystals in the N-doped carbonaceous bouquets.

Mo^{6+} (brown curve) from sample surface oxidation upon XPS analysis. There were three deconvoluted components in N 1s peak (Fig. S2, ESI†): the one at 394.6 eV is ascribed to Mo–N bonding; the other two at 398.1 and 401.1 eV are attributed to pyridinic N and graphitic N, respectively, consistent with the results for N-doped carbons reported previously.[35,36] Considering the higher intensity of Mo^{2+} peak than that of Mo^{3+} in Mo 3d spectrum and the weak N signal (Fig. S3, ESI†), we conclude that C species were more dominant than N species. Combining these results with the HRTEM images (Fig. 2d and e), the product was identified as N-dope carbon thin flakes embedded with small α-MoC$_{1-x}$ nanocrystals. Elemental mapping (Fig. 3f) further confirmed the uniform distribution and high density of α-MoC$_{1-x}$ nanocrystals in the N-doped carbonaceous bouquets.

For SSG applications, the α-MoC$_{1-x}$@CB product was fabricated into flat thin film by filtration method reported previously.[37] To accurately control the load of PCM on the film, the α-MoC$_{1-x}$@CB dispersion was diluted by a gradient to various concentrations (0.01–1.0 mg mL^{-1}), resulting in the flat films with gradually increased thickness (Fig. S4, ESI†) and the load of α-MoC$_{1-x}$@CB ranging from 0.008, 0.017, 0.033, 0.066, 0.083, 0.17, 0.50, to 0.83 mg cm^{-2}. The Ultraviolet-visible-near-infrared (UV-vis-NIR) reflection spectra (Fig. 4a) and transmission spectrum (Fig. S5, ESI†) showed broadband optical absorption over the whole solar spectrum (200–2500 nm) from all the α-MoC$_{1-x}$@CB flat films. Even when the load was as low as 0.066 mg cm^{-2}, the solar absorption efficiency reached ∼92%.

The performance of PCMs relies not only on their optical absorption property but also on the photothermal conversion capability. Rapidly-responsive temperature rise was seen from all the α-MoC$_{1-x}$@CB flat films (Fig. 4b and c). Even with an ultralow load of 0.066 mg cm^{-2}, equilibrium temperature of ∼80 °C was detected upon one-sun irradiation within as short as 60 s. As the commercial Nylon66 film (NF) was used as the filter and supporting layer beneath the PCM for the fabrication of the α-MoC$_{1-x}$@CB flat films (details in Methods, ESI†), the temperature variation of NF itself under one sun was recorded as a control, showing only a small rise of ∼7 °C even when irradiated for much extended duration, i.e. 900 s. Excitingly, when the load was reduced to 0.008 mg cm^{-2} (nearly two orders of magnitude lower than the commonly used PCM load in a SSG system),[20] a temperature elevation to 63 °C was still achieved within 60 s under one sun, evidently superior to the reported cases with much higher PCM load. For example, also under one sun, Ti$_2$O$_3$ NP[12] system with a load of ∼3.2 mg cm^{-2} rose to ∼52 °C after 700 s irradiation, hierarchically nanostructured gel[38] reached ∼45 °C after 500 s, and G1 MXene[20] nanocoatings with a load 0.32 mg cm^{-2} increased to 62.3 °C after 300 s. The powerful light-harvesting and photothermal conversion capabilities are not only attributed to the intrinsic optical nature of the nitrogen-doped carbon base and its combination with the high density of well-crystallized α-MoC$_{1-x}$ nanocrystals, but also to the 3D bouquet-like configuration, the highly porous structure, and the large specific surface area of α-MoC$_{1-x}$@CB.
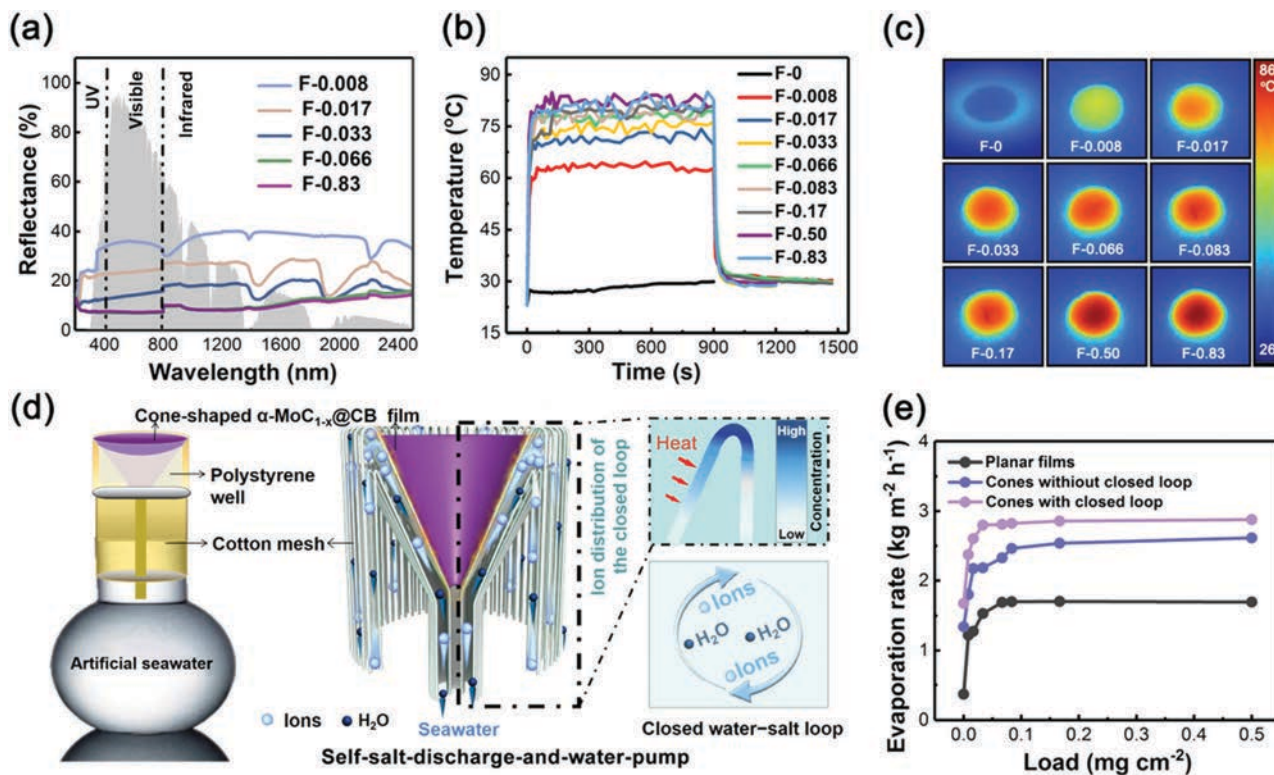
Fig. 4 Optical absorption, photothermal conversion and water evaporation performance of α-MoC$_{1-x}$@CB under one sun irradiation. (a) UV-vis-NIR reflection spectra of the α-MoC$_{1-x}$@CB flat films with different PCM loads. The grey background is the solar irradiation spectrum. F–X denotes the flat films, where X indicates the load of α-MoC$_{1-x}$@CB with the unit in mg cm^{-2}. (b) Time-dependent surface temperature and (c) infrared thermal images of the flat films with different α-MoC$_{1-x}$@CB loads, showing that α-MoC$_{1-x}$@CB can harvest and convert photon energy into heat efficiently even at a load as low as 0.033 mg cm^{-2} or lower. (d) Schematic illustration of the design of closed water–salt loop: the cone-shaped α-MoC$_{1-x}$@CB (purple) is located on a conformal polystyrene well (white) with their size matching the mouth of the seawater container (grey); a cotton rope (dark yellow) in a diameter of 2.5 mm is fixed at the cone's bottom and extended into the seawater; a cotton-mesh cylinder (pale gold) with one end attached to the cone's upper edge and the other end dipped in the bulk seawater is applied (the density of cotton mesh was 1.5 mg cm^{-2}). In this way, the cotton mesh acts as a bridge to discharge the salt from the high salinity area of the evaporator back to the bulk seawater, meanwhile faciliates more efficient water pumping together with the contribution of the cotton rope, driven by the salt concentration gradient. (e) Load-dependent water evaporation rate of the different setups, including the flat films, cone-shaped α-MoC$_{1-x}$@CB films with and without the closed water–salt loop, respectively, indicating that the cone-shaped evaporator can deliver higher evaporation rate compared with the 2D films, and the setup equipped with the cotton-mesh cylinder (i.e. with the water–salt loop) can further boost the solar evaporation performance.

We next carried out the hydrophilicity analysis based on surface contact angle measurements (Fig. S6, ESI†). It was revealed that the α-MoC$_{1-x}$@CB film was in a Janus form: whereas the Nylon66 side was hydrophilic, the PCM-loaded side remained super-hydrophobic even after 24 h constant desalination under one sun.

We then first evaluated the solar steaming performance of the flat α-MoC$_{1-x}$@CB films (with a diameter of 4.0 cm) floating on the surface of seawater (details in Methods, ESI†). Efficient solar steaming was demonstrated under one sun, in a load- and irradiation duration-dependent manner (Fig. S7, ESI†). For the film with a low load of 0.066 mg cm^{-2}, an evaporation rate as high as 1.70 kg m^{-2} h^{-1} was achieved, which was 4.6 folds higher than that of NF alone (0.37 kg m^{-2} h^{-1}). With an even lower load down to 0.033, 0.017 mg cm^{-2}, the evaporation rates (1.53, 1.27 kg m^{-2} h^{-1}) were still higher than those from the reported high-load SSG systems under the same irradiation intensity,[39] e.g. 0.80 kg m^{-2} h^{-1} from TiO$_x$[40] with a load $\sim$2.7 mg cm^{-2}, 1.24 kg m^{-2} h^{-1} from black amorphous

Al–Ti–O nanostructure.[41] Note that all solar-to-water conversion efficiencies presented here were calculated by subtracting the evaporation efficiency of seawater in dark, as shown in Fig. S8 (ESI†).

To further improve the evaporation performance, we constructed a 3D cone-shaped α-MoC$_{1-x}$@CB film, where the cone size matched exactly the container mouth (Fig. S9, ESI†) and the cone was placed in a polystyrene well (floating on the water surface) to enhance the heat localization effect. It is important to keep the cone size same as the dimension of water surface; otherwise, the evaporation performance could be overestimated. Due to the enlarged surface area and enhanced light-harvesting capability of the cone-shaped evaporator compared with the 2D flat film, the evaporation rate of this 3D evaporator was evidently improved (Fig. S10, ESI†). The rate increased from 1.70 to 2.61 kg m^{-2} h^{-1} (based on the projected area of the cone) with α-MoC$_{1-x}$@CB load of 0.50 mg cm^{-2}, and increased from 1.22 to 1.80 kg m^{-2} h^{-1} with an ultralow α-MoC$_{1-x}$@CB load of 0.008 mg cm^{-2}. However, pronounced salt

accumulation occurred at the upper edge of the cone after 12 h continuous desalination (Fig. S11, ESI†), although the evaporation rate can be maintained at ~ 2.60 kg m^{-2} h^{-1} over 60 h (Fig. S12, ESI†). Extending the desalination from 60 to 72 h, the salt-covered area spread from the edge to the whole cone (Fig. S11, ESI†), gradually reducing the effective work area and hence the photothermal conversion capability. Besides the initial salt precipitation observed at the cone's upper edge, the cone-edge preferential accumulation of salt is also confirmed by the direct demonstration in Video S1 and Fig. S13 (ESI†). Evident flow attributed to salt dissolution occurred specifically at the cone's upper edge when the cone-shaped evaporator flatly floated on deionized water surface after 4 h constant desalination in 20 wt% NaCl solution under one sun.

To solve the salt accumulation-induced issues, a hydrophilic cotton-mesh cylinder was applied with one end attached to the upper edge of the cone and the other end dipped in the seawater (Fig. 4d and Fig. S14, details in Methods, ESI†). The cylinder has the same diameter as the α-MoC$_{1-x}$@CB cone. As the salt preferentially precipitated at the cone edge, driven by the salt concentration gradient, the channels constructed *via* the cotton mesh can discharge the salt back to the bulk seawater meanwhile pumping water to the evaporator, forming a closed water–salt loop (Fig. 4d).

Thanks to this loop, the evaporation rate of seawater was further boosted for all given α-MoC$_{1-x}$@CB loads (Fig. 4e and Fig. S15, ESI†). For instance, even with an ultralow PCM load of 0.008 mg cm^{-2}, the water evaporation rate reached 2.4 kg m^{-2} h^{-1}, deducing a specific water evaporation rate as high as 24 kg m^{-2} h^{-1}·mg$_{PCMs}^{-1}$; with a low load of 0.033 mg cm^{-2}, the rate was 2.8 kg m^{-2} h^{-1}. Besides the enlarged evaporation area provided by the cotton-mesh cylinder, the evaporation enhancement is primarily attributed to the more powerful water pumping. As shown in Fig. S16 (ESI†), seawater can be suck upwards to the evaporator through the cotton rope at the cone bottom and the hydrophilic NF supporting film beneath the PCM layer, meanwhile the cotton-mesh cylinder can also transport seawater efficiently to the α-MoC$_{1-x}$@CB film to boost water pumping. To get better visual contrast, the seawater was dyed by rhodamine B.

We demonstrated the salt discharge capability of the loop as follows: the cone-shaped evaporator was placed in 20 wt% NaCl solution in a flask, the cotton mesh layer (with one end attached the cone's upper edge) was applied to cover the external surface of the flask, and the cotton-mesh covered flask was then dipped in deionized water (60 mL) in a beaker (Fig. 5a). After 12 h continuous desalination under one sun irradiation, the resistance of deionized water was measured to vary from 2.42 MΩ to 0.74 MΩ (Fig. S17, ESI†), providing the direct evidence for salt discharge from the cone edge to water through the cotton mesh. To quantify the salt discharge capability, we then evaluated the salinity of water in the beaker at several time points during a continuous desalination process. Briefly, 2 mL water was collected from the beaker every 12 h and dried in an oven for 24 h to evaluate the precipitated salt weight (Fig. 5b). As shown in Fig. 5c, after 60 h desalination

under one sun, the salt concentration in the beaker reached ~ 180 mg mL^{-1}.

The loop-equipped 3D evaporator is found to effectively solve the salt accumulation issue upon desalination. The cycling stability of this new SSG system was carefully evaluated under one sun illumination for 30 days (12 h continuous desalination per day). Remarkably, no salt accumulation occurred in the whole process; the high rate of evaporation was maintained over the month (Fig. 5d). Moreover, the product showed high storage stability: floating on the surface of seawater in a container constantly for over eight months (from December 2019 to August 2020), this SSG system showed no variation compared with a newly-produced one in terms of evaporation performance and appearance, without any sign of salt blockage. Besides desalination from regular seawater (3.5 wt%), sustainable SSG performance for highly concentrated solutions (20 wt% NaCl) is also crucial, yet certainly more challenging.[28] Excitingly, even upon continuous desalination in such concentrated seawater for over 400 h, the high evaporation rate of ~ 2.8 kg m^{-2} h^{-1} (under one sun) was successfully retained, showing no precipitated salt (Fig. 5e). To further demonstrate the salt discharge capability of our SSG system, higher irradiation power (three suns) was applied, that induced a much higher evaporation rate (6.0 kg m^{-2} h^{-1}). Even upon 12 h continuous desalination at such a high evaporation rate, no salt accumulation was induced as well (Fig. S18, ESI†).

The salinity level of the evaporated water is another critical factor to evaluate desalination efficacy. For an accurate evaluation, we set up a 4×3 array of 3D α-MoC$_{1-x}$@CB cones (with the loop applied and the PCM load of 0.066 mg cm^{-2}) floating on the seawater surface in a container (Fig. S19, ESI†). The whole system was then sealed in a glass chamber and placed in an ice bath (Fig. S20, ESI†). Based on the analysis of inductively-coupled plasma mass spectrometry, the concentrations of four primary ions in the condensed water, including Na$^+$, K$^+$, Mg^{2+}, and Ca^{2+}, were all reduced by over three orders of magnitude as compared with the initial concentrations of the artificial seawater (Fig. 5f). The resultant salinity level well complied with the standard for healthy drinking water, that defined by the World Health Organization (WHO) and the US Environmental Protection Agency (EPA).

Discussion

Due to the enlarged evaporation area and light-harvesting capability compared with 2D flat films, the advantage of 3D SSG systems in terms of the evaporation rate has been widely documented.[22,23,42–46] However, when applied to solar desalination, the cone-shaped evaporators are not suitable, due to the particularly serious salt blockage of the setup.[26,43,45] Consistently, without the water–salt loop, pronounced salt accumulation also occurred in our case, and preferentially began from the upper edge of the cone-shaped α-MoC$_{1-x}$@CB evaporator (Fig. S11, ESI†). This phenomenon indicates the inhomogeneous salt concentration at the different areas of the cone, with that at the upper edge higher than the rest region
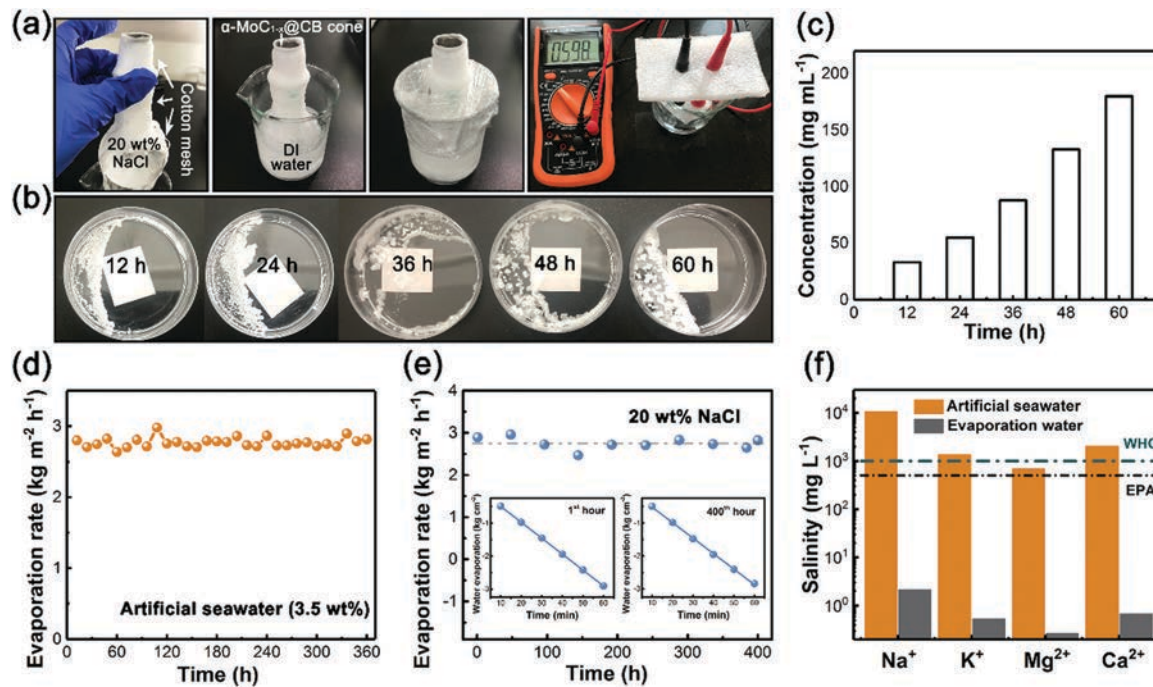
2456 | *Energy Environ. Sci.*, 2021, **14**, 2451–2459

This journal is © The Royal Society of Chemistry 2021

Fig. 5 Salt discharge and long-term desalination enabled by the water–salt loop. (a) Photographs of the setup for direct demonstration for the salt discharge capability of the loop: the cotton-mesh cylinder (with one end attached to the cone's edge) covers the external flask surface, the flask is dipped in deionized water in a beaker, and the beaker is then covered by polyethylene film to reduce the influence of natural evaporation. The density of cotton mesh of 4.0 mg cm^{-2}. The resistance of water in the beaker reflecting the salt concentration discharged from the cone to water is measured using a multimeter with a constant distance between the electrodes. (b) Photographs of precipitated salt obtained by drying the solution (2 mL) from beaker at different evaporation time points. (c) Time-dependent salt concentration of water in beaker (under one sun). (d) Cycling stability in the regular artificial seawater (3.5 wt%). The SSG cycling was performed under one sun illumination for 30 days (12 h continuous desalination per day), showing enduring and steady desalination performance. (e) 400 h continuous desalination for the highly concentrated salt solution (20 wt% NaCl). Comparing the performance at the 1st h with that at the 400th h (the two insets), no evaporation decline was induced. (f) The measured concentration of four primary metal ions in the regular artificial seawater (yellow) and the evaporated water by solar desalination using the present SSG system (grey), indicating that the sanity of the latter is much better than the standard defined by WHO and EPA.

(Fig. S13 and Video S1, ESI†).[43,45] When the cotton-mesh cylinder was constructed with one end attached to the cone upper edge and the other end dipped into bulk seawater, a direct bridge between the high and low salinity areas was established. Driven by the concentration gradient, salt can then be discharged from the evaporator back to the bulk seawater through the connection.

Meanwhile, this setup facilitated more efficient water pumping: aside from water pumping *via* the NF supporting film and cotton rope attached at the cone's bottom (Fig. 4d), the cotton-mesh cylinder can draw more water towards the evaporator due to its hydrophilicity, capillarity, as well as the salt concentration gradient between its two ends. Combining the boosted water pumping with the further enlarged evaporation area by the cylinder, the evaporation rate increased (Fig. 4e). The density of the cotton-mesh cylinder had to be optimized to obtain the best solar desalination performance: when the density was too low, salt accumulation occurred due to the insufficient salt discharge; when density was too high, the evaporation rate was reduced, because the high-density cotton held too much water that can distract quite a percentage heat induced by photothermal conversion. The optimized cotton-mesh density was associated with the irradiation condition, which was

1.5 mg cm^{-2} and 4.0 mg cm^{-2} for one and three sun irradiation, respectively.

The implementation of simultaneous desalination sustainability and high evaporation rate depends not only on the smart setup of the salt–water loop but also on the distinct nature of our PCM, *i.e.* α-MoC$_{1-x}$@CB. First, its super-hydrophobicity (Fig. S6, ESI†) made it impossible for seawater to enter the PCM layer; water evaporation then occurred at the interface between the hydrophobic PCM layer and the hydrophilic NF layer beneath it, avoiding salt precipitation in the PCM layer. Note that although the PCM layer is protected from salt in this case, steam release is compromised. A PCM layer as thin and porous as possible is thus highly desirable to achieve an efficient path for water evaporation. However, the optical absorption and photothermal conversion capability of PCMs rely strongly on the PCM load (the thickness of PCM layer) in most cases:[20,47,48] the evaporation rate can be greatly decreased with just a little smaller PCM load. Remarkably, α-MoC$_{1-x}$@CB presented strong and broad absorption over the whole solar spectrum, and reached rather high equilibrium temperatures (*e.g.* ~80 °C) within a very short time (*e.g.* 60 s) upon one-sun irradiation, even with an ultralow load of 0.033–0.066 mg cm^{-2} (Fig. 4a–c). Such a load efficiency is important not only in terms

This journal is © The Royal Society of Chemistry 2021

Energy Environ. Sci., 2021, **14**, 2451–2459 | **2457**

of the cost efficiency hence practicability for real-life desalination, but also because it allows the very thin PCM layer (thickness of $\sim$1–3 μm corresponding to the load of 0.033–0.066 mg cm^{-2}, Fig. S4, ESI†) to be competent for SSG. Meanwhile, the thin and porous petals and typical 3D framework of the bouquet-like α-MoC$_{1-x}$@CB provided the rapid path for water vapor.

Conclusions

We present a solution for preventing salt accumulation for SSG from seawater, resulting in steady and high-rate evaporation without salt precipitation not only upon the long cycling (30 days) in regular seawater, but also upon continuous desalination in the highly concentrated salt solution ($>$400 h) or at a high evaporation rate (6.0 kg m^{-2} h^{-1}). The excellent performance is attributed to the joint contribution of the salt–water loop and the desirable nature of α-MoC$_{1-x}$@CB: the former enables self salt discharge and water pump; the latter endows broad and strong optical absorption over the full solar spectrum, high-yield (1300 mg$_{\text{α-MoC}_{1-x}@\text{CB}}$ g$_{\text{Mo}}^{-1}$) and rapid photothermal conversion as well as a shortcut for vapor release that leads to the high evaporation rate, and super-hydrophobicity and fast vapor diffusion together strengthern the salt resistence. The strategy provided in this work solves the top challenge for sustainable solar desalination, and may inspire the development of a variety of advanced SSG systems with both high evaporation rate and long-term operation life.

Author contributions

L. Z., M. Y., and Y. S. designed the project; L. Z. synthesized and characterized the α-MoC$_{1-x}$@CB and evaluated the SSG performance of α-MoC$_{1-x}$@CB; L. Z. and H. Z. carried out SEM analysis; L. Z., L. S. and Y. S. analyzed and interpreted the results; M. Y., L. Z., F. R. and H. A. wrote or/and edited the manuscript; M. Y. and Y. H. supervised the project.

Conflicts of interest

There are no conflicts to declare.

Acknowledgements

References

1 M. A. Shannon, P. W. Bohn, M. Elimelech, J. G. Georgiadis, B. J. Marinas and A. M. Mayes, *Nature*, 2008, **452**, 301.

2 L. Zhou, Y. Tan, J. Wang, W. Xu, Y. Yuan, W. Cai, S. Zhu and J. Zhu, *Nat. Photonics*, 2016, **10**, 393.

3 M. Elimelech and W. A. Phillip, *Science*, 2011, **333**, 712.

4 X. Zhou, F. Zhao, Y. Guo, Y. Zhang and G. Yu, *Energy Environ. Sci.*, 2018, **11**, 1985.

5 E. Chiavazzo, M. Morciano, F. Viglino, M. Fasano and P. Asinari, *Nat. Sustain.*, 2018, **1**, 763.

6 G. Ni, G. Li, S. V. Boriskina, H. Li, W. Yang, T. Zhang and G. Chen, *Nat. Energy*, 2016, **1**, 16126.

7 P. Tao, G. Ni, C. Song, W. Shang, J. Wu, J. Zhu, G. Chen and T. Deng, *Nat. Energy*, 2018, **3**, 1031.

8 F. Zhao, Y. Guo, X. Zhou, W. Shi and G. Yu, *Nat. Rev. Mater.*, 2020, **5**, 388.

9 T. A. Cooper, S. H. Zandavi, G. W. Ni, Y. Tsurimaki, Y. Huang, S. V. Boriskina and G. Chen, *Nat. Commun.*, 2018, **9**, 5086.

10 K. Bae, G. Kang, S. K. Cho, W. Park, K. Kim and W. J. Padilla, *Nat. Commun.*, 2015, **6**, 10103.

11 S. Yu, Y. Zhang, H. Duan, Y. Liu, X. Quan, P. Tao, W. Shang, J. Wu, C. Song and T. Deng, *Sci. Rep.*, 2015, **5**, 13600.

12 J. Wang, Y. Li, L. Deng, N. Wei, Y. Weng, S. Dong, D. Qi, J. Qiu, X. Chen and T. Wu, *Adv. Mater.*, 2017, **29**, 1603730.

13 L. Sun, Z. Li, R. Su, Y. Wang, Z. Li, B. Du, Y. Sun, P. Guan, F. Besenbacher and M. Yu, *Angew. Chem., Int. Ed.*, 2018, **57**, 10666.

14 H. Liu, C. Chen, H. Wen, R. Guo, N. A. Williams, B. Wang, F. Chen and L. Hu, *J. Mater. Chem. A*, 2018, **6**, 18839.

15 K.-T. Lin, H. Lin, T. Yang and B. Jia, *Nat. Commun.*, 2020, **11**, 1389.

16 H. Ghasemi, G. Ni, A. M. Marconnet, J. Loomis, S. Yerci, N. Miljkovic and G. Chen, *Nat. Commun.*, 2014, **5**, 4449.

17 X. Hu, W. Xu, L. Zhou, Y. Tan, Y. Wang, S. Zhu and J. Zhu, *Adv. Mater.*, 2017, **29**, 1604031.

18 H. Geng, Q. Xu, M. Wu, H. Ma, P. Zhang, T. Gao, L. Qu, T. Ma and C. Li, *Nat. Commun.*, 2019, **10**, 1512.

19 L. Zhang, B. Tang, J. Wu, R. Li and P. Wang, *Adv. Mater.*, 2015, **27**, 4889.

20 K. Li, T.-H. Chang, Z. Li, H. Yang, F. Fu, T. Li, J. S. Ho and P.-Y. Chen, *Adv. Energy Mater.*, 2019, **9**, 1901687.

21 B. Zhu, H. Kou, Z. Liu, Z. Wang, D. K. Macharia, M. Zhu, B. Wu, X. Liu and Z. Chen, *ACS Appl. Mater. Interfaces*, 2019, **11**, 35005.

22 C. Tu, W. Cai, X. Chen, X. Ouyang, H. Zhang and Z. Zhang, *Small*, 2019, **15**, 1902070.

23 G. Chen, N. Zhang, N. Li, L. Yu and X. Xu, *Adv. Mater. Interfaces*, 2019, **7**, 1901715.

24 Y. Bian, Q. Du, K. Tang, Y. Shen, L. Hao, D. Zhou, X. Wang, Z. Xu, H. Zhang, L. Zhao, S. Zhu, J. Ye, H. Lu, Y. Yang, R. Zhang, Y. Zheng and S. Gu, *Adv. Mater. Technol.*, 2019, **4**, 1800593.

25 H. Ren, M. Tang, B. Guan, K. Wang, J. Yang, F. Wang, M. Wang, J. Shan, Z. Chen, D. Wei, H. Peng and Z. Liu, *Adv. Mater.*, 2017, **29**, 1702590.

26 L. Wu, Z. C. Dong, Z. R. Cai, T. Ganapathy, N. X. Fang, C. X. Li, C. L. Yu, Y. Zhang and Y. L. Song, *Nat. Commun.*, 2020, **11**, 521.

27 M. Zhu, Y. Li, F. Chen, X. Zhu, J. Dai, Y. Li, Z. Yang, X. Yan, J. Song, Y. Wang, E. Hitz, W. Luo, M. Lu, B. Yang and L. Hu, *Adv. Energy Mater.*, 2018, **8**, 1701028.

2458 | *Energy Environ. Sci.*, 2021, **14**, 2451–2459

This journal is © The Royal Society of Chemistry 2021

28 X. Dong, L. Cao, Y. Si, B. Ding and H. Deng, *Adv. Mater.*, 2020, **32**, 1908269.

29 S. He, C. Chen, Y. Kuang, R. Mi, Y. Liu, Y. Pei, W. Kong, W. Gan, H. Xie, E. Hitz, C. Jia, X. Chen, A. Gong, J. Liao, J. Li, Z. J. Ren, B. Yang, S. Das and L. Hu, *Energy Environ. Sci.*, 2019, **12**, 1558.

30 C. Xiao, W. Liang, L. Chen, J. He, F. Liu, H. Sun, Z. Zhu and A. Li, *ACS Appl. Energy Mater.*, 2019, **2**, 8862.

31 W. Xu, X. Hu, S. Zhuang, Y. Wang, X. Li, L. Zhou, S. Zhu and J. Zhu, *Adv. Energy Mater.*, 2018, **8**, 1702884.

32 Y. Kuang, C. Chen, S. He, E. M. Hitz, Y. Wang, W. Gan, R. Mi and L. Hu, *Adv. Mater.*, 2019, **31**, 1900498.

33 Y. Xia, Q. Hou, H. Jubaer, Y. Li, Y. Kang, S. Yuan, H. Liu, M. W. Woo, L. Zhang, L. Gao, H. Wang and X. Zhang, *Energy Environ. Sci.*, 2019, **12**, 1840.

34 T. Li, W. Luo, H. Kitadai, X. Wang and X. Ling, *Adv. Mater.*, 2019, **31**, 1807160.

35 Z. Zhou, Z. Yuan, S. Li, H. Li, J. Chen, Y. Wang, Q. Huang, C. Wang, H. E. Karahan, G. Henkelman, X. Liao, L. Wei and Y. Chen, *Small*, 2019, **15**, 1900358.

36 M. Li, Y. Zhu, H. Wang, C. Wang, N. Pinna and X. Lu, *Adv. Energy Mater.*, 2019, **9**, 1803185.

37 L. Zhu, L. Sun, H. Zhang, D. Yu, H. Aslan, J. Zhao, Z. Li, M. Yu, F. Besenbacher and Y. Sun, *Nano Energy*, 2019, **57**, 842.

38 F. Zhao, X. Zhou, Y. Shi, X. Qian, M. Alexander, X. Zhao, S. Mendez, R. Yang, L. Qu and G. Yu, *Nat. Nanotechnol.*, 2018, **13**, 489.

39 X. Zang, C. Jian, T. Zhu, Z. Fan, W. Wang, M. Wei, B. Li, M. Follmar Diaz, P. Ashby, Z. Lu, Y. Chu, Z. Wang, X. Ding, Y. Xie, J. Chen, J. N. Hohman, M. Sanghadasa, J. C. Grossman and L. Lin, *Nat. Commun.*, 2019, **10**, 3112.

40 M. Ye, J. Jia, Z. Wu, C. Qian, R. Chen, P. G. O'Brien, W. Sun, Y. Dong and G. A. Ozin, *Adv. Energy Mater.*, 2017, **7**, 1601811.

41 L. Yi, S. Ci, S. Luo, P. Shao, Y. Hou and Z. Wen, *Nano Energy*, 2017, **41**, 600.

42 W. Li, Z. Li, K. Bertelsmann and D. E. Fan, *Adv. Mater.*, 2019, **31**, 1900720.

43 Y. Wang, C. Wang, X. Song, M. Huang, S. K. Megarajan, S. F. Shaukat and H. Jiang, *J. Mater. Chem. A*, 2018, **6**, 9874.

44 Y. Shi, R. Li, Y. Jin, S. Zhuo, L. Shi, J. Chang, S. Hong, K.-C. Ng and P. Wang, *Joule*, 2018, **2**, 1171.

45 N. Cao, S. Lu, R. Yao, C. Liu, Q. Xiong, W. Qin and X. Wu, *Chem. Eng. J.*, 2020, **397**, 125522.

46 X. Li, R. Lin, G. Ni, N. Xu, X. Hu, B. Zhu, G. Lv, J. Li, S. Zhu and J. Zhu, *Natl. Sci. Rev.*, 2018, **5**, 70.

47 R. Li, L. Zhang, L. Shi and P. Wang, *ACS Nano*, 2017, **11**, 3752.

48 G. Cheng, X. Wang, X. Liu, Y. He and B. V. Balakin, *Sol. Energy*, 2019, **194**, 415.

This journal is © The Royal Society of Chemistry 2021

Energy Environ. Sci., 2021, **14**, 2451–2459 | **2459**